Biomacromolecules

Open Access

pubs.acs.org/Biomac

Article

Analysis of PTEN Antagonistic Peptides (PAPs) in Neuronal Growth and Traumatic Brain Injury (TBI)

Karla K. Rivera,[⊥] Yu-Liang Tsai,[⊥] Jialei Song, Hao Gu, Anne-Sophie Gutt, Daniela Sinske, Claudia Klugmann, Marica Pagliarini, Francesco Roselli, Christopher V. Synatschke,* and Bernd Knöll*

Cite This: *Biomacromolecules* 2026, 27, 5419−5431

Read Online

ACCESS | Metrics & More | Article Recommendations | Supporting Information

ABSTRACT: PTEN (phosphatase and tensin homologue) is an established cellular growth brake whose inhibition stimulates regeneration of injured neurons in rodent models. Herein, we employed peptide-based PTEN inhibition targeting PTEN's phosphatase activity. Therefore, a fusion peptide (PAP2-TAT) of PAP2 (PTEN antagonistic peptide 2) with TAT (transactivator of transcription) was used to enable cellular entry. PAP2-TAT was not cytotoxic and entered the cytoplasm of primary mouse neurons, where it enhanced neurite growth, growth cone size, and synaptophysin abundance. PAP2-TAT modestly elevated P-AKT and more strongly elevated P-ERK levels. Furthermore, STATs (signal transducer and activator of transcription) were phosphorylated after PAP2-TAT administration. So far, PAPs have not been employed in traumatic brain injury (TBI). In a mouse TBI model, a single PAP2-TAT injection improved single parameters of gait impairments but had no impact on neuroinflammation and TBI-associated weight loss. In summary, peptide-based PTEN inhibition aids neuronal cell growth and regeneration after brain injury.

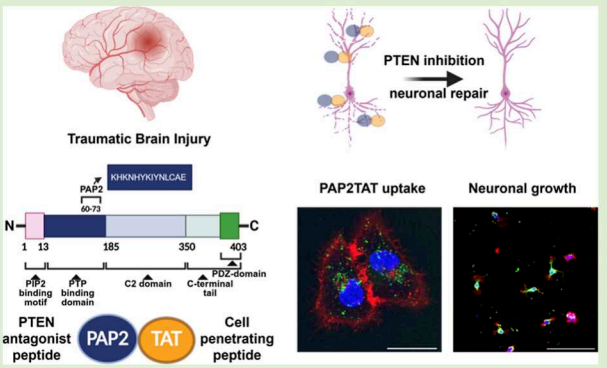

INTRODUCTION

PTEN is a dual-specific lipid and protein phosphatase operating as an essential inhibitor of cell growth and survival by counteracting PI3 kinase activity. Given PTEN's function as a cellular growth brake, targeted PTEN inhibition reproducibly stimulated diverse aspects of cell growth.[1,2] In neurons, genetic PTEN ablation resulted in hypertrophy of cell somata[3,4] and growth cones,[5,6] more dendritic arborizations,[7,8] neurite growth,[9−11] and enhanced circuit formation and activity.[12,13] This might impede physiological brain function in mouse models, resulting in epilepsy.[14] Importantly, after neuronal injury, PTEN deletion enhanced axonal regeneration and recovery.[15,16] This was shown in several mouse models of spinal cord,[17,18] traumatic brain,[19−22] and peripheral nerve[4,9] injury.

To unlock PTEN's therapeutic potential, several pharmacological approaches including compound- and peptide-based PTEN inhibition have been reported.[16,23] Compounds targeting PTEN such as bisperoxovanadium (bpV) block PTEN function but also target other enzymes and have side effects such as modulating blood glucose levels.[24] In this study, peptide-based inhibition of PTEN was employed. In previous studies, so-called PTEN antagonist peptides (PAPs) targeting several PTEN functional domains including phosphatase activity were reported.[18] For PAPs to function as an intracellular PTEN antagonist, conjugation with the TAT sequence (transactivator of transcription) is used to facilitate PAP cell entry.[25] PAP-TATs were already successfully applied in rodent models of spinal cord injury: systemic PAP injection enhanced sprouting of cortico- and bulbospinal fibers and enhanced recovery of locomotor function in mouse models of spinal cord injury.[25−29] Moreover, PAPs enhanced neuronal growth in culture and elevated P-AKT levels.[25]

So far, PAP-based PTEN inhibition has not been tested in mouse models of traumatic brain injury (TBI). Since in TBI neuronal connections are directly severed by the mechanical injury, we thought to enhance neuronal growth and regeneration by PAP2-mediated PTEN inhibition. For this, we employed a mouse TBI model of closed-head injury inducing TBI through a weight-drop apparatus.[30] PAP2 is derived from PTEN's phosphatase (PTP) domain (amino acids 60−73) and was previously shown to bind the PTEN protein.[25] In addition, PAP application downregulates PTEN protein abundance in primary neurons.[26] PAP2-TAT was locally applied to the lesion site, and functional recovery

Received: March 31, 2026
Revised: June 30, 2026
Accepted: June 30, 2026
Published: July 10, 2026

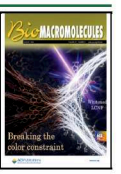

Table 1. Name, Peptide Sequence, and Molecular Weight of the Peptides Used for This Study

name	sequence	M_w
TAT	RKKRRQRRR	1338.7
FITC-TAT	FITC-AhxRKKRRQRRR	1841.2
PAP2	KHKNHYKIYNLCAE	1761.0
FITC-PAP2	FITC-AhxKHKNHYKIYNLCAE	2263.6
PAP2-TAT	KHKNHYKIYNLCAERKKRRQRRR	3081.7
FITC-PAP2-TAT	FITC-AhxKHKNHYKIYNLCAERKKRRQRRR	3584.2

through CatWalk XT analysis of gait parameters was applied. Indeed, specific gait parameters impaired by TBI were modestly improved by PAP2-TAT application. In addition, PAP2-TAT enhanced primary neuronal growth, growth cone area, and presynaptic marker abundance. Mechanistically, we found modulation of MAP kinase and STAT signaling by PAP-TAT.

In summary, this study further supports the proregenerative activity of PTEN inhibition through peptide-based PTEN interference.

EXPERIMENTAL SECTION

Materials and Methods

Solid-Phase Peptide Synthesis and Peptide Modification. All the peptides were synthesized using the Fmoc (Fluorenylmethoxycarbonyl)-SPPS method on 100−200 mesh resins in an automated microwave peptide synthesizer (Liberty Blue, CEM Corporation) from the C- to N-terminus. DMF (*N*,*N*-dimethylformamide) was used as the main washing solvent, and the deprotection solvent was a mixture of 20% piperidine in DMF. The activator and activator base were 0.5 M DIC (*N*,*N*′-diisopropylcarbodiimide) and 1.0 M Oxyma (Ethyl cyano(hydroxyimino)acetate), both in DMF. The amount of materials and reagents was prepared in accordance with the calculation performed by the Liberty Blue software, and the procedure is described briefly as follows. Rink Amide resin beads were swollen in DMF for 30 min prior to synthesis and then again in the automatic synthesizer for an additional 10 min. An additional spacer Fmoc aminohexanoic acid (Ahx) was inserted at the N-terminus for all fluorescein-labeled (FITC) peptides. Single amino acid coupling was routinely applied, unless otherwise stated. The procedure began with Fmoc removal. The resin beads were immersed in the deprotection solvent and heated to 75 °C (155 W) for 15 s, followed by 90 °C (30 W) for 50 s. The beads were then washed twice with DMF. Subsequently, the respective amino acid (at a concentration of 0.2 M) was coupled in DMF with the assistance of an activator and an activator base. The reaction mixture was heated to 75 °C (170 W) for 15 s and then to 90 °C (30 W) for 110 s, after which it was flushed with DMF. Arginine (Fmoc-Arg-Pbf−OH) underwent double coupling. Coupling of histidine (Fmoc-His-Trt−OH) was carried out at 25 °C for 120 s and 50 °C (35 W) for 480 s. Deprotection solvent was added to remove the Fmoc motif after the final coupling. FITC-labeling was done manually at the N-terminus on resin beads with a stoichiometry of 1:2:4 (peptide: FITC: DIPEA, diisopropylethylamine) in DMF in a peptide reactor (Carl Roth) for 4 h at room temperature (RT). Afterward, the resin beads were first rinsed with DCM (dichloromethane) to unreacted chemicals and were immersed in a cleavage cocktail 95% TFA (Trifluoroacetic acid), 2.5% Milli-Q water, and 2.5% TIPS (Triisopropylsilane) for 2 h. The crude product was obtained by precipitation in cold diethyl ether and centrifugation. The amino acid sequences are listed in Table 1 and the mechanisms for FITC-labeling are depicted in Figure S1.

Purification and Characterization of Peptides. The peptide precipitates were dissolved in a mixture of Milli-Q H_2O and ACN (acetonitrile) and purified by preparative reverse-phase high-performance liquid chromatography (HPLC; Shimadzu) via a C18 column (Phenomenex Gemini, 5 μm, NX-C18, 110 Å, 150 × 30 mm) at a flow rate of 25 mL/min. Samples were collected in fractions based on chromatography, which was monitored using an ultraviolet (UV) absorption detector at 214 nm. The purified samples were lyophilized and stored at −20 °C prior to use.

The samples were identified by matrix-assisted laser desorption/ionization-time-of-flight mass spectrometry (MALDI-TOF MS) via the dried droplet method. The samples were mixed with a saturated solution of the matrix CHCA (cyano-4-hydroxycinnamic acid; Milli-Q H_2O/ACN 1:1 + 0.1% TFA). MALDI-TOF spectra were recorded using a rapifleX MALDI-TOF/TOF instrument (Bruker).

The purity of the samples was confirmed by analytical reverse-phase HPLC. The analytical HPLC (Shimadzu) system was equipped with a C18 column (ZORRBAX Eclipse XDB-C18, 5 μm, 70 Å, 9.4 × 250 mm) at a flow rate of 4 mL/min. The eluent was a solvent mixture of ACN/Milli-Q acidified with 0.1% TFA, ranging from 5% to 80% ACN. The samples were monitored using UV absorption at 214 nm.

Cell Viability and Cellular Uptake. To study the potential cytotoxicity and cellular uptake of PAP2-TAT, SH-SY5Y cells (human neuroblastoma cell) were incubated at 37 °C and 5% CO_2 in Dulbecco's Modified Eagle Medium (DMEM)/Nutrient Mixture F-12 (F-12), supplemented with 10% fetal bovine serum (FBS) and 1% penicillin−streptomycin (PS), to study the potential cytotoxicity and cellular uptake of PAP2-TAT. The cells were seeded at a density of 5000 cells/well in a 96-well plate and incubated at 37 °C for 24 h. Peptide powders were dissolved in DMSO (dimethyl sulfoxide) and further diluted in the culture medium. The cells were treated with different concentrations (0.1, 0.33, 0.66, 1.0, 3.3, 6.6, 10, 33, 66, and 100 μM) of PAP2-TAT (50 μL) at 37 °C for 24 h. Cell viability was assessed using the GloMax-MultiDetector System and CellTiter-Glo Assay according to the manufacturer's protocol. The reagent (50 μL) was added to each well plate, which was gently shaken for 2 min. The plate was incubated for an additional 10 min in the dark at room temperature prior to measurement.

Cellular uptake of the peptides was performed using SH-SY5Y cells with the same cell culture procedure. The cells were seeded at a density of 40,000 cells/well in an 8-well plate (μ-Slide 8 Well Glass Bottom, Ibidi) for 24 h. Subsequently, the cells were treated with10 μM of FITC-PAP2-TAT or FITC-PAP2 in culture medium at 37 °C for 24 h. After incubation, each well was gently washed to remove any excess compounds. To improve the visualization of cellular uptake, the cell nuclei were stained with Hoechst 33342 dye (Thermo Fisher Scientific), and the cell membranes were stained with a deep red plasma membrane stain (Invitrogen).

Primary Neuronal and Organotypic Cultures. C57BL/6J pups (postnatal day 0−2) were sacrificed by decapitation directly into ice-cold PBS. The hippocampi were isolated in ice-cold HBSS (Hank's balanced salt solution), then digested in 0.05% Trypsin−EDTA for 10 min at 37 °C. Following digestion, tissues were washed twice with prewarmed HBSS and subsequently incubated in 1 mL of DMEM supplemented with 10% FBS to inactivate trypsin. Tissues were gently dissociated with a full-diameter, flame-polished Pasteur pipet tip, followed by a half-diameter, flame-polished pipet tip for 1 min each. The resulting cell suspension was spun down at 600 rpm for 7 min. After removing the supernatant, the cell pellet was resuspended in fresh culture media. Cells were counted with a Neubauer chamber and plated at a density of 5000 cells/well into peptide-supplemented media at a concentration of 3 μM in 96-well glass-bottom plates (P96−1.5H−N, Celvis). Plates were left uncoated, except for PLL/laminin controls, which were coated with poly-*L*-lysine (10 μg/mL;

https://doi.org/10.1021/acs.biomac.6c00695
Biomacromolecules 2026, 27, 5419−5431

P6282, Sigma-Aldrich) and mouse laminin (20 μg/mL, L2020, Sigma-Aldrich). Cultures were maintained in a humidified incubator kept at 37 °C and 5% CO_2 and stained after 24 h in culture for all experiments. For long-term (14 DIV, days in vitro) cultures, plates were additionally coated with PLL to ensure cell attachment.

Immunocytochemistry. Cells were washed with ice-cold PBS (phosphate-buffered saline) and fixed in 4% PFA +5% glucose in PBS for 15 min at RT. After washing three times with PBS, cells were permeabilized with 0.1% Triton-X-100 in PBS for 5 min at RT. Cells were washed two more times in PBS and allowed to block for 30 min in 2% BSA in PBS before incubating with βIII tubulin (0.28 μg/mL, PRB-435P, TUJ1; Covance), MAP2 (1:3000, Cat# CPCA-MAP2, EnCor), Synaptophysin1 (2 μg/mL, p38−1,101,308, Synaptic Systems), or P-STAT5A/B (1.5 μg/mL, Cat No. 12071-1, Proteintech) for 1 h at room temperature. Cells were washed three times with PBS and then incubated for 1 h in the dark at RT with Alexa-488 donkey anti-rabbit (2 μg/mL, A21206, Thermo Fisher), Alexa-488 donkey anti-chicken (0.67 μg/mL, A-78948, Invitrogen), Alexa-546 goat anti-mouse (2 μg/mL, A11003, Invitrogen), CF633 donkey anti-guinea pig (2 μg/mL, 20171, Biotium), and Phalloidin Texas Red (1 U/mL, #00033, Biotium). Cells were washed twice with PBS and incubated for 5 min with DAPI (1:2000 dilution in PBS). DAPI was replaced with 1% PFA in 1.25% sucrose in PBS.

Immunoblotting. Neuronal cell cultures were maintained for 24 h before being stimulated with 3 μM of peptides for 30 min and 25 ng/mL of BDNF (brain-derived neurotrophic factor). Protein lysates were prepared from cells or tissues using freshly made ice-cold lysis buffer (100 μL per 35 mm dish of primary neurons, 150 μL for tissue), followed by incubation and scraping on ice. Lysates were rotated for 30 min at 4 °C, centrifuged (13,000*g*, 2 min, 4 °C), and protein concentrations were determined by Bradford assay (0.5% lysate with 20% Rothi-Quant in PBS, absorbance at 595 nm). Equal amounts of protein (30 μg) were denatured and separated by SDS-PAGE using hand-cast resolving and stacking gels prepared in the Bio-Rad casting equipment. After polymerization, gels were run with protein ladders for 20 min at 50 V and 125 min at 135 V. Proteins were transferred to methanol-activated PVDF membranes (90 min, 80 V, 4 °C) in prechilled transfer buffer with an ice pack to maintain low temperature. Membranes were stained with Ponceau S to verify transfer, washed in TBST (Tris-buffered saline with Tween), and blocked for 30 min in 5% milk (or BSA, when required). After blocking, membranes were incubated with primary antibodies *p*-AKT (Ser473) (1:1000, 4060, Cell Signaling), AKT (pan) (1:1000, 4691S, Cell Signaling), *p*-ERK 1/2 (1:1000, 4370, Cell Signaling), ERK 1/2 (1:1000, 9102, Cell Signaling), and GAPDH (1:5000, 3683, Cell Signaling) overnight at 4 °C, washed three times with TBST, and subsequently incubated with HRP-conjugated secondary antibodies (1:5000 in 5% milk/TBST) for 1 h at room temperature. Following additional TBST washes, membranes were incubated with a freshly prepared ECL substrate and imaged using a ChemiDoc system (Bio-Rad). Chemiluminescent TIFF images were imported into ImageJ for quantification. Lanes were aligned and defined using the gel analysis tool, peak areas corresponding to protein bands were measured after background subtraction, and values were exported to Excel. Phosphorylated protein intensities were normalized first to GAPDH, then to the corresponding total protein, and phospho/total ratios were calculated to compare experimental treatments.

Phospho-Array. Primary hippocampal neurons from P0−P2 mice were maintained for 24 h and incubated at 37 °C and 5% CO_2. Cultures from a total of 20 mice were pooled to obtain sufficient material for two conditions (PAP2-TAT and DMSO; $N = 1$ each). Phospho antibody array, comprised of 304 antibodies from 16 commonly studied signaling pathways, was performed using the Full Moon BioSystems kit (Cat #: PCS300; Full moon Biosystems) according to the manufacturer's protocol.

According to the antibody array assay kit, neurons were washed three times with ice-cold PBS, lysed in 50 μL/well nondenaturing extraction Buffer (supplemented with protease/phosphatase inhibitors), scraped, and pooled (3 wells/condition). Lysis beads were added, followed by five cycles of vigorous vortexing (1 min) and ice incubation (10 min), with sequential centrifugation (10,000*g*, 5 min; 18,000*g*, 20 min; 4 °C) to yield clarified supernatants. Protein lysates (30−100 μg) were adjusted to 75 μL of Labeling Buffer, biotinylated with biotin reagent (1−2 h, RT, intermittent mixing), and stopped with stop reagent. Antibody array slides were blocked (30 min, orbital shaker) with blocking solution, rinsed extensively with deionized water, and then incubated with diluted biotinylated samples (6 mL coupling solution, 1 h, RT, gentle shaking). Arrays were washed (3× in 1× wash solution) and rinsed, followed by 20 min incubation with Cy3-streptavidin diluted in detection buffer (RT, dark), additional washes, and drying (1000*g* centrifugation). Slides were scanned at 10 μm resolution in the Cy3 channel using an Affymetrix microarray scanner, and signal intensities were quantified with the manufacturer-provided GAL (GenePix Array List) file and microarray analysis software. Array spots were identified semiautomatically and manually corrected where necessary. Signal intensities were extracted using GenePix Pro 6.1 software. For each slide, the median intensity value of each spot was obtained, and the average of the five replicate spots was used for downstream analysis. Data were normalized to β-tubulin and expressed as fold change.

Weight-Drop TBI Model and Peptide Injection. Mice were individually anesthetized with 5% sevoflurane (800 mL/min O_2) in an induction chamber, then maintained at 3.5% via mask after confirming loss of pedal withdrawal reflex; analgesia was administered subcutaneously (buprenorphine, 0.04 mg/kg). Scalps were shaved, disinfected, and incised (1 cm midline) to expose the skull, with bregma marked. Heads were secured in the weight-drop apparatus, eyes protected with Bepanthen salve, and the impactor positioned flush with motor cortex (0.5 mm posterior, 1.5 mm left of bregma). A 120 g weight was released from a 40 cm height (2.25 mm depth limit via a spacer) to induce focal TBI. Postimpact, mice received immediate oxygen and cardiac massage and were stabilized under 3.5% sevoflurane and transferred to stereotaxic injection. For injections, glass capillaries (1 mm; World Precision Instruments) were pulled, backfilled, loaded with 2 μL of 10 μM peptide or vehicle (DMSO), and mounted on a Hamilton syringe (RN compression fitting) in a stereotaxic frame. A 0.5 mm hole was drilled at the impact site (Foredom rotary tool, Meisinger carbide bur), cleaned with cotton swabs, and the capillary was lowered into the cortex at a depth of 0.2 mm for stepwise injection during withdrawal. Scalps were sutured, and mice were recovered in a heated transport cage. Sham animals received the same treatment as TBI-treated mice except for the TBI weight-drop impact.

Animals and treatments were randomized, and the experimenter was blinded to the group allocation.

Behavior. To assess gait and motor coordination post-TBI and peptide treatments, mice underwent habituation and testing with the CatWalk XT system (a glass walkway with a tunnel used to observe gait deficits). All behavior tests were performed 2−3 days prior to the TBI, followed by 1, 3, 5, and 7 days post injury as before.[31]

Immunohistochemistry. Immunohistochemistry was performed on paraffin-embedded tissue sections to visualize antigens and identify cell types. Slides were dewaxed overnight at 60 °C, then rehydrated through sequential incubations: xylene (2 × 5 min), 100% EtOH (5 min, 3 min), 90% EtOH (2 min), 70% EtOH (2 min), followed by two washes in ddH_2O (2 min each). Antigen retrieval was achieved by pressure cooking slides in citrate buffer for 10 min, followed by 10 min cooling and a 1 min ddH_2O wash. Tissue was circled with a PAP pen, blocked with 2% BSA in TBS (30 min, RT), and incubated overnight at RT with 80−100 μL/slide of primary antibodies NeuN (1 μg/mL, MAB377, Millipore), GFAP (2 μg/mL, ab4674, Abcam), and Iba1 (2 μg/mL, 019−19741, WAKO). The next day, slides were washed in TBST (10 min), incubated with secondary antibodies (1:500, 30 min, RT, dark), washed again in TBST (10 min), stained with DAPI (5 min, dark), and washed once more in TBST (10 min). Slides were briefly dipped in ddH_2O, air-dried (20−30 min, RT), and mounted with Mowiol under glass coverslips.

Quantification and Statistics. High-throughput primary neuronal outgrowth scans were analyzed using a neural network designed and provided by Evident Scientific using the scanR 3.1 Analysis

https://doi.org/10.1021/acs.biomac.6c00695
Biomacromolecules 2026, 27, 5419−5431

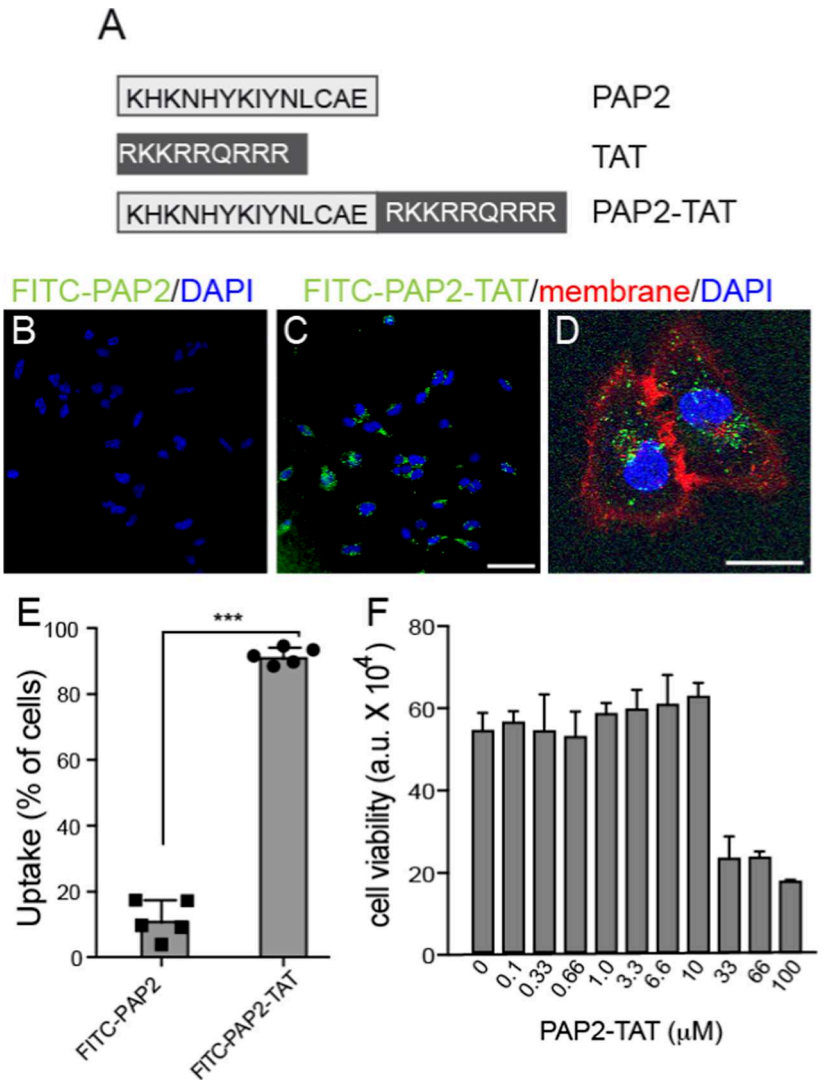

Figure 1. PAP2-TAT has low cytotoxicity and is efficiently taken up by cells. (A) 1-letter amino acid sequences of the peptides employed in the study. (B–E) FITC-conjugated PAP2 alone did not enter SH-SY5Y cells (B), whereas PAP2-TAT labeled with FITC was found in the majority of cells (C). Higher magnification revealed cytoplasmic abundance of PAP2-TAT inside cells (D). Quantification revealed that approximately 90% of cells were PAP2-TAT positive (E). (F) Cell viability of SH-SY5Y cells was not affected by PAP2-TAT concentrations between 0.1 and 10 μM. Higher concentrations resulted in some cytotoxicity. For statistical analysis in (E), a one sample *t*-test was performed, and significance was calculated in relation to FITC-PAP2 (*, **, and *** reflecting $P \leq 0.05$, 0.01, and 0.001). Circles or squares depict independent cultures analyzed. Scale-bar (B,C) = 50 μm; (D) = 20 μm.

Software. Nonhigh-throughput cultures and brain sections were analyzed manually with custom ImageJ macros.

Statistical analysis was conducted using a one-sample *t*-test, or one-way ANOVA followed by Kruskal–Wallis test and Dunn's multiple comparisons test, depending on the normality and homogeneity of variance. Data containing two independent variables were analyzed using two-way ANOVA with interaction terms and appropriate post hoc tests. Significance is denoted as $^{*}P \leq 0.05$, $^{**}P \leq 0.01$, and $^{***}P \leq 0.001$. Data are depicted as mean ± SD if not indicated otherwise.

RESULTS

Synthesis and Characterization of Peptides

In this study, we combined the previously published PAP2 sequence[25] with a TAT sequence (see Table 1 and Figure 1A). The TAT sequence in this study was shortened by four amino acids compared to a previous report[25] by omitting one amino acid at the N-terminus and three at the C-terminus (see Table 1). FITC labeling of the peptide was performed on resin with an additional Ahx spacer on the N-terminus to prevent side reactions upon TFA cleavage.[32] Following the coupling reactions, the resin beads were rinsed with DCM, immersed in the cleavage cocktail, and precipitated in a cold diethyl ether. The crude peptides were dissolved in a mixture of Milli-Q H_2O and ACN before being purified and collected by RP-HPLC. The purity of each compound was further confirmed by analytical HPLC (Figure S2), which showed that compounds were highly pure (purity >95%). The different retention times of each compound can be explained by the interaction between the compounds and the column. The more polar the compound is, the earlier it is eluted from the column.[33] This is consistent with the sequences containing the highly polar TAT group eluting earlier than the other compounds. Conversely, fluorophore-labeled compounds containing relatively hydrophobic dyes were eluted later on the same column. The MALDI-TOF MS of each compound shows the expected mass-to-charge (m/z) ratio (Figure S3).

https://doi.org/10.1021/acs.biomac.6c00695
Biomacromolecules 2026, 27, 5419–5431

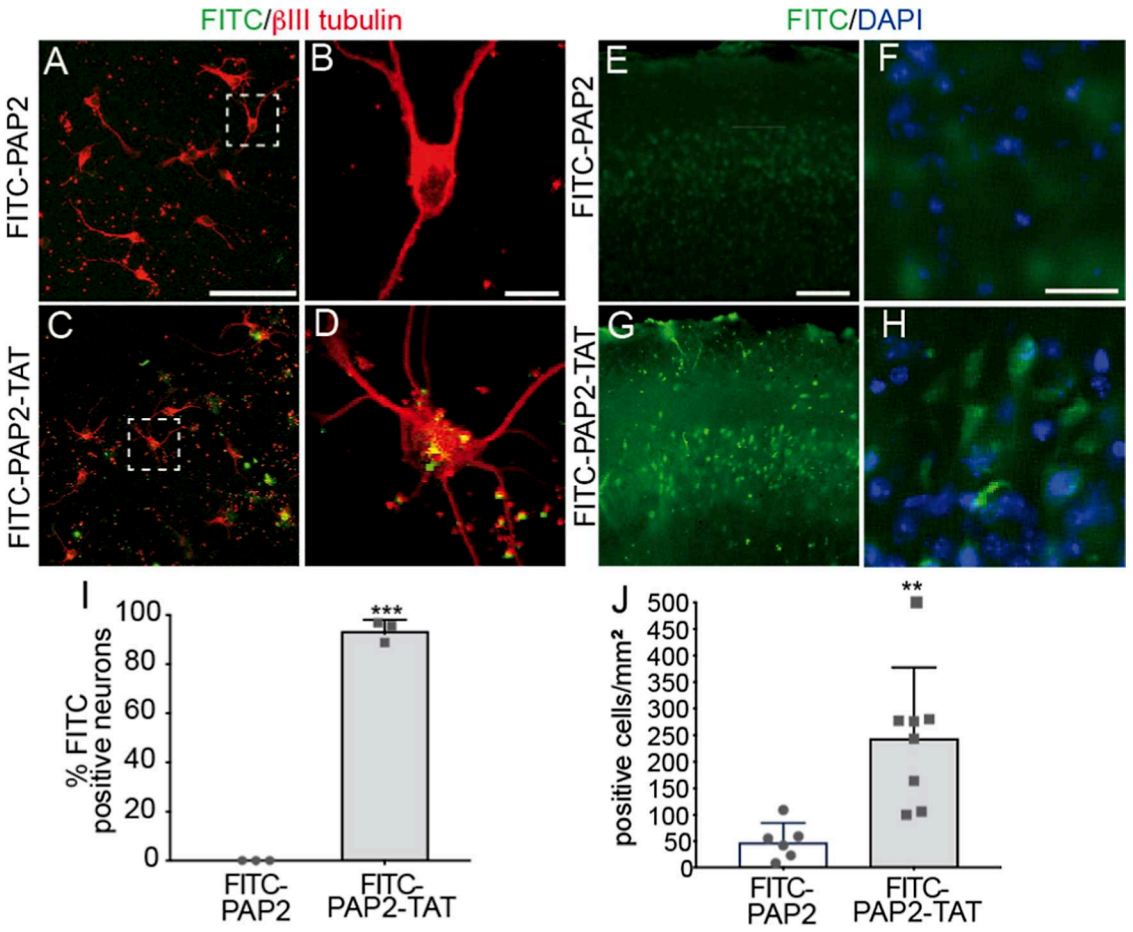

Figure 2. PAP2-TAT enters primary cultured mouse neurons (A–D). FITC-PAP2 was not found in mouse primary hippocampal neurons (A,B). In contrast, FITC-PAP2-TAT-positive signals were found in neurons (C,D). Dashed areas in (A,C) indicate higher magnifications presented in (B, D). (E–H) Mouse cortical brain slices were incubated with FITC-PAP2 (E,F) or FITC-PAP2-TAT (G,H). FITC-PAP2-TAT was clearly present in neuronal layers of the cortex (G,H). In contrast, only weak signals were observed for FITC-PAP2 (E,F). (I,J) Quantification of the percentage of FITC-positive cells for primary hippocampal neurons (I) or cortical brain slices (J). Circles or squares depict independent cultures analyzed. For statistical analysis in (I,J), a one sample *t*-test was performed, and significance was calculated in relation to FITC-PAP2 (*, **, and *** reflecting $P \leq 0.05$, 0.01, and 0.001). Scale-bar (A, C, E, G) = 100 μm; (B, D) = 10 μm; (F, H) = 25 μm.

PAP2-TAT Does Not Impair Cell Viability and Is Taken Up by Different Cell Types

The cellular uptake and concentration range of peptide administration tolerable by cells were analyzed in SH-SY5Y cells (Figure 1).

To measure cellular uptake, 10 μM of FITC-conjugated PAP2-TAT or—as control—PAP2 alone conjugated with FITC (FITC-PAP2) was added to the growth medium (Figure 1B–E). There was no green fluorescent signal from the FITC-PAP2-treated group, indicating that FITC-PAP2 could not enter the cytoplasm (Figure 1B, E). In contrast, FITC-PAP2-TAT entered almost 90% of all cells (Figure 1C, E) and was present throughout the cytoplasm (Figure 1D).

Next, cell viability was assessed using an adenosine triphosphate (ATP)-based luminescent assay (Figure 1F). We did not observe an impact of PAP2-TAT on cell viability in a concentration range between 0.1 μM and 10 μM (Figure 1F). However, a higher concentration of PAP2-TAT induced cytotoxicity in SH-SY5Y cells (Figure 1F). Taken together, a concentration of up to 10 μM of PAP2-conjugated peptides was tolerable to cells, and a concentration of 10 μM resulted in efficient cytoplasmic transfer.

Since we aimed at analyzing PAP2-TAT's impact on neuronal growth, we investigated the efficiency of cellular uptake in mouse primary neuronal and organotypic culture (Figure 2). As observed for SH-SY5Y cells (Figure 1), FITC-PAP2 alone conjugated to FITC did not enter βIII tubulin-positive neurons (Figure 2A, B, I). In contrast, FITC-PAP2-TAT conjugated with FITC was found in mouse primary hippocampal neurons with approximately 90% of cells being positive (Figure 2C, D, I). To analyze uptake in an in vivo-related model, we employed mouse cortical organotypic slices preserving the cortical architecture for some time in culture (Figure 2E–H; J). As before, almost no FITC-PAP2 was present in cortical neurons (Figure 2E,F; J). However, addition of TAT to PAP2 allowed for entry into cortical neurons in brain slices (Figure 2G,H; J).

In summary, PAP2-TAT was also present in the primary mouse neurons.

PAP2-TAT Stimulates Primary Neuronal Growth and Enhances Growth Cone Size and Presynaptic Marker Abundance

In the next step, the potential of PAP2-TAT to stimulate neuronal growth was tested (Figure 3). For this, mouse primary hippocampal neurons were plated on uncoated

https://doi.org/10.1021/acs.biomac.6c00695
Biomacromolecules 2026, 27, 5419–5431

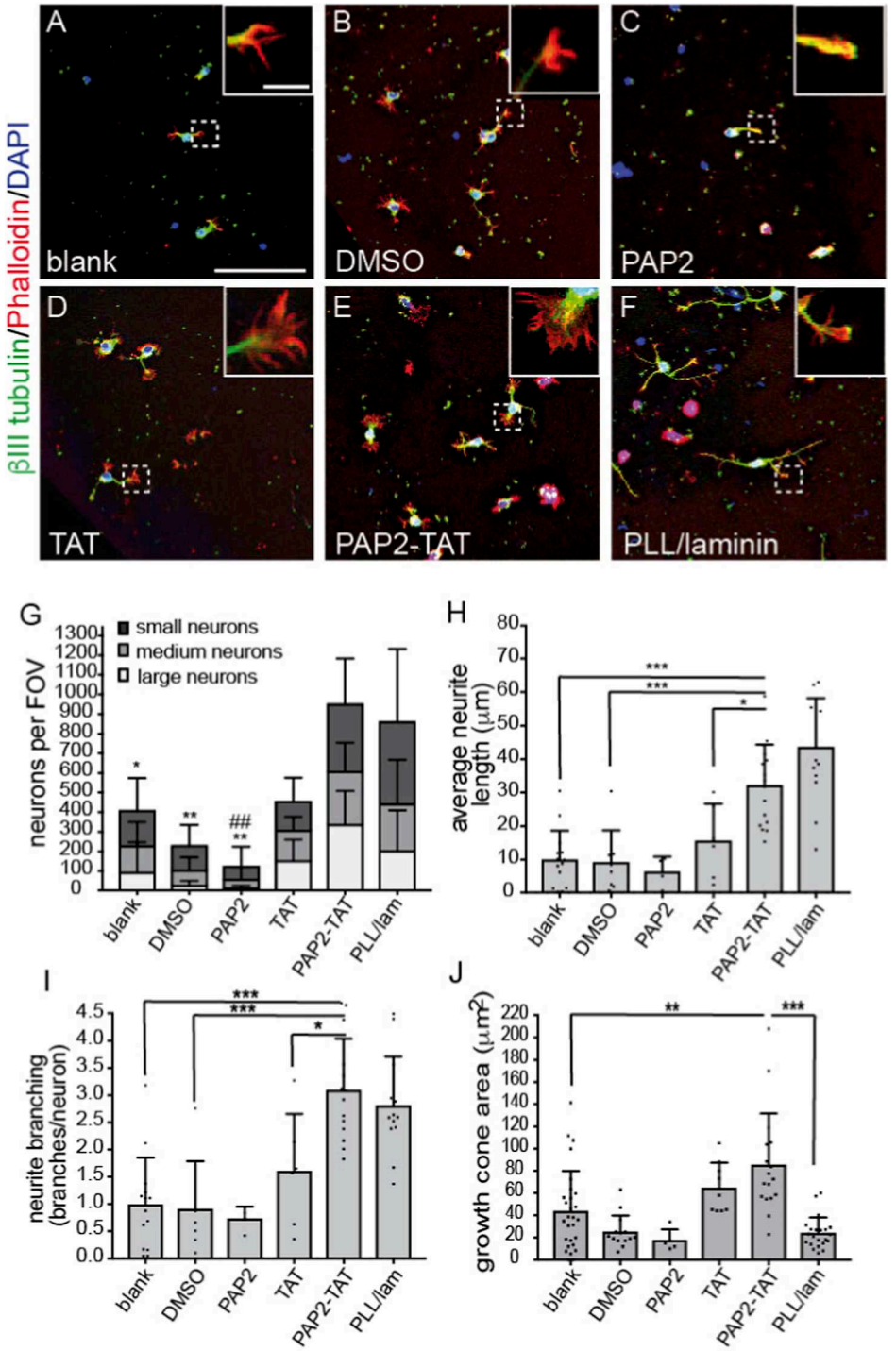

Figure 3. PTEN inhibition by PAP2-TAT enhances neurite growth and growth cone size in primary neurons (A–F). Primary mouse hippocampal neurons were plated on glass coverslips with no coating (A–E) or coated with PLL/laminin (F). PAP2-TAT (E) added to the growth medium enhanced numbers of neurons with growth, average neurite length, and branching in relation to blank (A), DMSO (B), PAP2 (C), and TAT (D). Insets revealed higher magnifications of growth cones labeled with dashed boxes. Growth cones of neurons treated with PAP2-TAT had the largest area (E). (G–J) Quantification of three size categories of neurons (small, medium, large) per field of view (FOV; G). PAP2-TAT incubation resulted in comparable values obtained with the growth permissive substrate PLL/laminin (G). The PLL/laminin substrate achieved the highest average neurite length with PAP2-TAT almost reaching similar neurite length (H). The number of neurite branches/neurons was also elevated by PAP2-TAT similarly as PLL/laminin (I). PAP2-TAT-mediated PTEN inhibition resulted in the largest areas of growth cones (J). Each dot in (H and I) represents one culture analyzed (N = 4–16). In each culture, >50 neurons were analyzed. In (J), each dot represents one independent culture (N = 4–16) with 10–30 growth cones analyzed per culture. In each culture, 3–6 animals were pooled. For statistical analysis in (G), an ordinary two-way ANOVA with Dunnett's multiple comparisons test and a single pooled variance was performed. For (H–J), an ordinary one-way ANOVA with Tukey's multiple comparisons test with a single pooled variance was performed, and significance is indicated relative to FITC-PAP2 (*, **, and *** reflecting $P \leq 0.05$, 0.01, and 0.001; $^{\#\#}$ reflects $P \leq 0.01$). In (G), asterisks provide significance in relation to PAP2-TAT for large neurons, whereas "#" refers to small neurons. Scale-bar (A–F) = 100 μm; (insets A–F) = 10 μm.

https://doi.org/10.1021/acs.biomac.6c00695
Biomacromolecules 2026, 27, 5419–5431

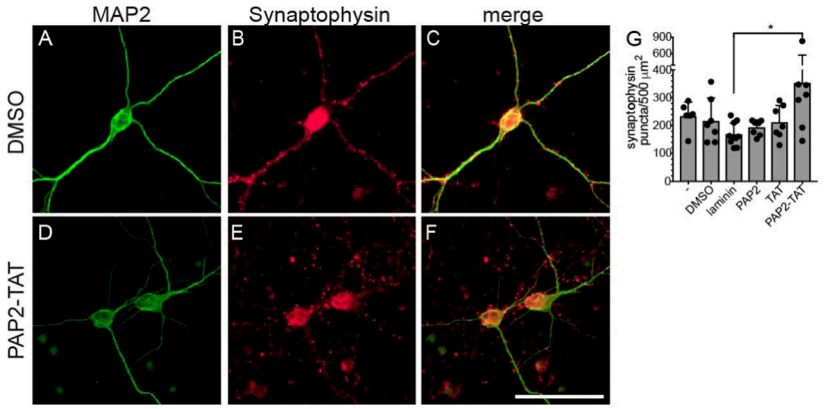

Figure 4. PTEN inhibition increases the abundance of presynaptic marker synaptophysin along neurites (A−F). Primary mouse hippocampal neurons were stained for the dendrite marker MAP2 (green) and the presynaptic marker synaptophysin (red). Synaptophysin puncta were elevated by PAP2-TAT incubation (D−F) in comparison with DMSO (A−C). (G) Quantification of synaptophysin puncta/area revealed significantly highest numbers obtained by PAP2-TAT incubation, whereas PAP2 or TAT peptides resulted in comparable levels to DMSO. Each dot in (G) represents one independent culture with >20 neurons analyzed per coverslip. Each experiment consisted of pooled tissue from 3 to 6 animals. For statistical analysis in (G), a one-way ANOVA with Kruskal−Wallis test and Dunn's multiple comparisons test was performed, and significance is indicated by *, **, and *** reflecting $P \leq 0.05$, 0.01, and 0.001. Scale-bar (A−F) = 30 μm.

coverslips to provide a growth-restrictive environment (Figure 3A−E). As a positive control, coverslips were coated with PLL and laminin (PLL/lam; Figure 3F), thereby providing a growth-permissive substrate reflecting the optimal neuronal growth achievable.

Neurons incubated with no peptide (blank; Figure 3A) or DMSO to account for the peptide solvent used (Figure 3B) expectedly resulted in poor neuronal growth (Figure 3G−I). Neuronal growth was quantified by three parameters including numbers of small, medium, or large-sized neurons/area (Figure 3G), average neurite length (Figure 3H), and number of branches/neuron (Figure 3I). Similarly, PAP2 alone did not enhance any of the growth parameters compared to blank or DMSO (Figure 3C,G−I). The TAT sequence alone was also analyzed and resulted in a slight but not significant increase in neurite length (Figure 3D,H). However, TAT alone also significantly enhanced the neurite branching activity. This suggests some biological activity exerted by the TAT peptide alone (Figure 3D,I). In accordance with this, in a single study available in the literature so far which analyzed unconjugated TAT peptide alone, TAT-associated neuroprotective activities were reported.[34]

PAP2-TAT addition to primary neurons grown on uncoated coverslips (Figure 3E) resulted in stimulation of numbers of neurons with outgrowth (Figure 3G), elevated average neurite length (Figure 3H), and branching (Figure 3I). Notably, effects obtained with PAP2-TAT were comparable to the results of the positive control, i.e., neurons grown on PLL/laminin (Figure 3G−I).

An important neuronal structure is a growth cone elaborated at the neurite tip involved in axon guidance during brain development and axonal injury.[35] Growth cones are F-actin-rich structures that can be visualized with phalloidin recognizing F-actin. Previously, PTEN inhibition was associated with the hypertrophy of cellular structures.[36] Thus, we wondered whether growth cone size might likewise be affected by PAP2-mediated PTEN inhibition (insets Figure 3A−F; J). Indeed, administration of PAP2-TAT (inset Figure 3E) resulted in almost twice the growth cone area compared to blank (Figure 3A), DMSO (Figure 3B), and PAP2 (Figure 3C; quantified in J). TAT alone (Figure 3D) also elevated growth cone size, albeit not to the same extent as PAP2-TAT (Figure 3J). This suggests some biological cellular activity of the TAT sequence alone, as noticed above. Notably, PLL/laminin (Figure 3F) did not raise growth cone size (Figure 3J), suggesting a PAP2-TAT-specific activity on growth cones.

PTEN-deficiency in the nervous system was previously connected to circuit assembly and neuronal activity in mice.[13] We analyzed a putative role of peptide-based PTEN inhibition in presynaptic marker abundance in early differentiation stages of mouse hippocampal cultures (Figure 4). For this, MAP2, a marker of dendrites, was used to label neurons along with synaptophysin, labeling presynaptic structures of synapses (Figure 4A−F). PAP2-TAT (Figure 4D−F) enhanced the number of synaptophysin puncta in comparison to control treatments including no addition ("-"), DMSO (Figure 4A−C), PAP2 or TAT alone, and laminin (Figure 4G). Thus, interfering with PTEN resulted in elevated numbers of presynaptic structures along MAP2-positive neurites.

In summary, peptide-mediated PTEN inhibition enhanced neuronal growth, growth cone size, and synaptophysin puncta.

PAP2-Mediated PTEN Inhibition Upregulates MAP Kinase and STAT Signaling

To investigate underlying signaling alterations caused by PTEN interference, we performed immunoblotting for phosphorylated AKT and ERK (P-AKT and P-ERK; Figure 5A−C). For this, primary hippocampal neurons were incubated with TAT alone or three different concentrations of PAP2-TAT (1 μM, 3 μM, 10 μM; Figure 5A−C). In addition, BDNF (brain-derived neurotrophic factor) was used as positive control known to activate ERK and AKT. When normalized to GAPDH and total AKT levels, PAP2-TAT did not result in consistent P-AKT upregulation (Figure 5A,B). In contrast, 1 and 3 μM PAP2-TAT did induce P-ERK which was not observed for TAT alone (Figure 5A, C). Thus, PTEN inhibition augmented ERK phosphorylation more strongly than P-AKT levels.

In addition to known PTEN signaling targets, a protein phosphor-array for more global alterations of phosphorylated and total abundance of signaling proteins induced by PTEN inhibition was performed (Figure 5D). For this, primary mouse hippocampal neurons were maintained for 24 h before being

https://doi.org/10.1021/acs.biomac.6c00695
Biomacromolecules 2026, 27, 5419−5431

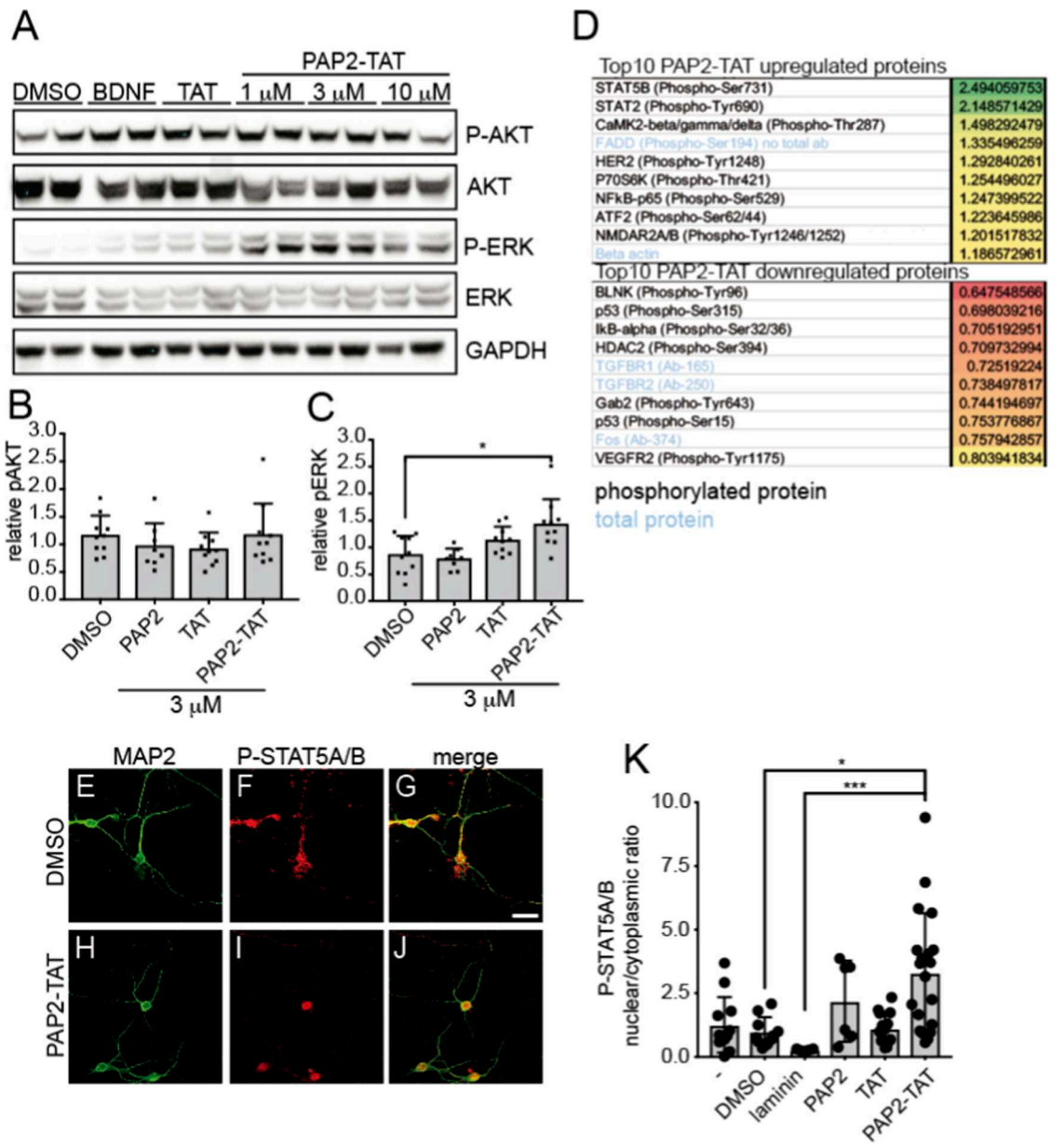

Figure 5. Elevated P-ERK and P-STAT levels after PAP2-TAT application in neurons. (A) Protein lysates of primary mouse hippocampal neurons were immunoblotted with antibodies directed against P-AKT and P-ERK along with antibodies recognizing total AKT and ERK levels. P-AKT levels were weakly modulated by PAP2-TAT application, whereas P-ERK levels were increased. (B,C) Quantification of P-AKT (B) and P-ERK (C) levels relative to total AKT or ERK at 30 min of stimulation with 3 μM of peptide concentrations. Each dot in (B) or (C) indicates one independent culture analyzed. (D) Protein phospho-arrays were incubated with primary hippocampal neuron lysates, and Top10 up- and downregulated proteins by PAP2-TAT were depicted. P-STAT5B and P-STAT2 showed the strongest induction by PAP2-TAT. (E−K) Primary mouse hippocampal neurons were incubated with DMSO (E−G) or PAP2-TAT (H−J) followed by labeling neurons with MAP2 and phosphorylation status of STAT5A/B. PAP2-TAT significantly elevated the nuclear abundance of P-STAT5A/B in relation to control treatments (K). Each dot in (K) depicts one independent culture analyzed. For statistical analysis in (B, C, and K), a one-way ANOVA with Kruskal−Wallis test and Dunn's multiple comparisons test was performed, and significance is indicated by *, **, and *** reflecting $P \leq 0.05$, 0.01, and 0.001. Data are depicted as mean ± SEM. Scale-bar (E−J) = 10 μm.

stimulated for 30 min with 3 μM of PAP2-TAT or DMSO. Thereafter, protein lysates were added to the array slides coated with antibodies. Out of the 304 proteins recognized by the protein array antibodies, we found that among the top 10 PAP2-TAT upregulated phospho-sites were P-STAT5A/B and P-STAT2 (Figure 5D). For downregulated phospho-sites, the B cell linker protein (BLNK) was the top hit among the 10 most regulated proteins (Figure 5D). To confirm upregulation of P-STAT proteins by PAP2-TAT-mediated PTEN inhibition, we employed primary hippocampal neurons (Figure 5E−J; K). Indeed, PAP2-TAT but neither PAP2 nor TAT alone upregulated the nucleus to cytoplasmic ratio of P-STAT5A/B (Figure 5E−J; K), therefore corroborating protein phosphor-array results (Figure 5D).

PTEN Inhibition by PAP2-TAT Modulates and Improves Selected TBI-Affected Parameters

Previously, PTEN inhibition with PAP peptides successfully improved recovery in mouse spinal cord injury models.[25,26,28]

https://doi.org/10.1021/acs.biomac.6c00695
Biomacromolecules 2026, 27, 5419−5431

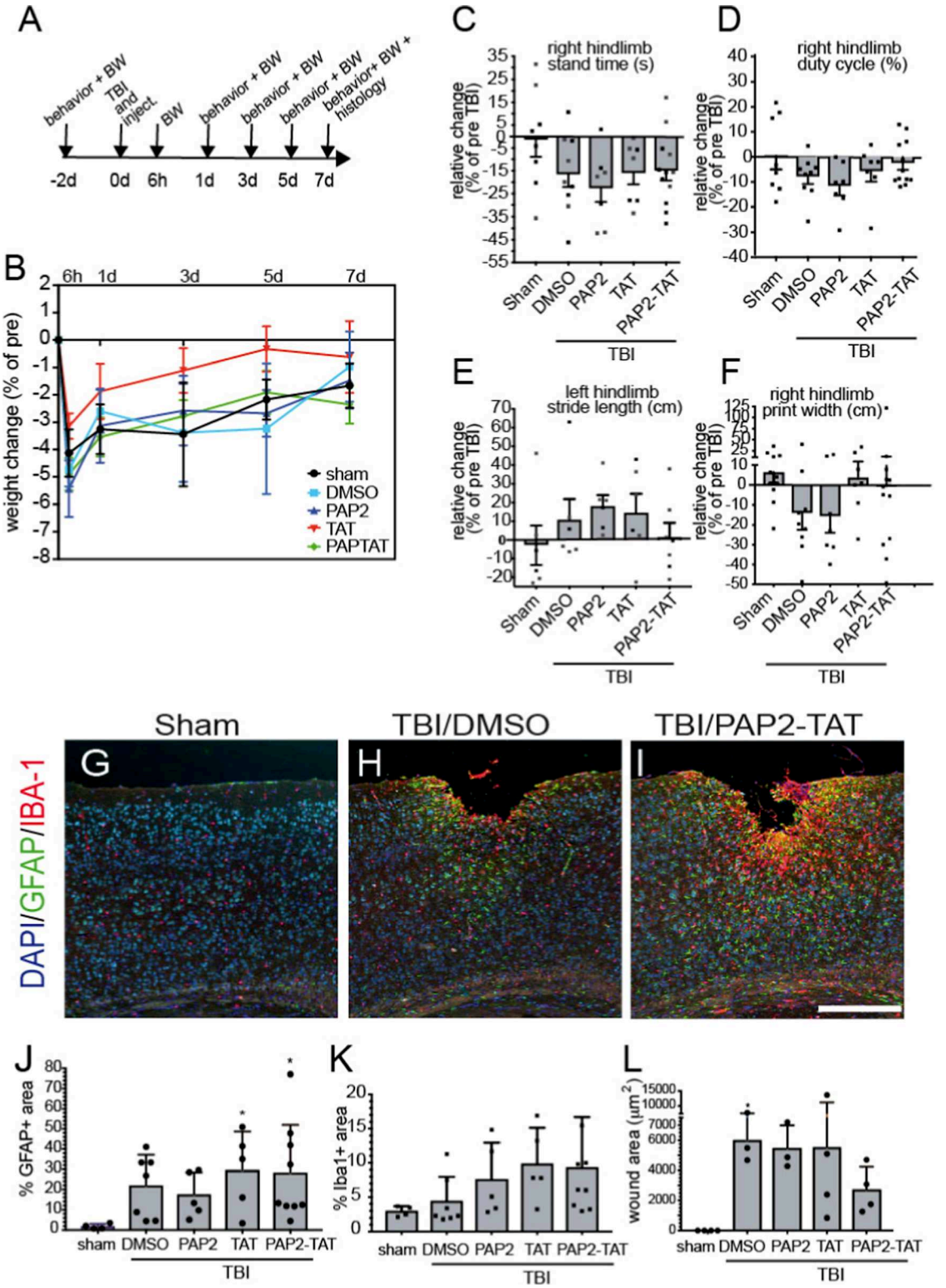

Figure 6. Analysis of PAP2-TAT injection in a mouse TBI model. (A) Outline of the experimental scheme with time line. BW reflects body weight measurement. (B) Body weight decreased after TBI or sham treatment in all cohorts in relation to body weight measured before ("pre") TBI/sham intervention. Zero change in body weight over the 7 days is reflected by a straight line. Animals receiving a single TAT peptide injection had at all time points the least weight reduction although with no statistical significance. (C−F) CatWalk XT analysis of four different gait parameters at 1 day post TBI or sham treatment. All changes are provided in relation to values obtained before ("pre") TBI or sham surgery. TBI reduced the stand time of the hindlimbs in relation to sham surgery with no obvious impact by any of the treatments (C). The duty cycle was reduced by TBI with the highest reduction obtained in DMSO, PAP2, and TAT groups (D). Animals with a single PAP2-TAT injection after TBI had values comparable to sham-treated animals (D). Stride length (E) was elevated by TBI in relation to sham in all groups except for PAP2-TAT. The hindlimb print width was reduced in DMSO and PAP2 groups after TBI in relation to sham which was not observed in animals injected with either PAP2 or PAP2-TAT (F). Each square in (C−F) reflects one mouse analyzed. (G−L) Cortical brain sections at 7 days post sham (G) or TBI (H,I)

https://doi.org/10.1021/acs.biomac.6c00695
Biomacromolecules 2026, 27, 5419−5431

Figure 6. continued

treatment were stained for astrocyte (GFAP$^+$, green) or microglia (IBA-1$^+$, red) abundance. After TBI, both inflammatory cell types were induced in relation to sham (G), however without any difference between DMSO (H) or PAP2-TAT (I) administration. GFAP- (J) or IBA1-positive (K) area in the cortex was quantified for all conditions. The cortical wound area (L) was elevated by TBI with the smallest wound area measured after PAP2-TAT-mediated PTEN inhibition (I, L). In (J, K, L), each dot or square reflects one animal analyzed. For each readout in Figure 6, $N = 7-12$ animals/condition. For statistical analysis in (B), an ordinary two-way ANOVA with Dunnet's multiple comparisons test and a single pooled variance was performed, and in (C−L), a one-way ANOVA with Tukey's multiple comparisons test with a single pooled variance was performed, and significance is indicated by *, **, and *** reflecting $P \leq 0.05$, 0.01, and 0.001. (G−L) Scale-bar (G−I) = 100 μm.

So far, peptide-mediated PTEN inhibition has not been employed in rodent TBI models.

In a next step, we used a weight-drop mouse closed head TBI model to analyze PAP2-TAT's impact in post-TBI recovery (Figure 6). For this, mice were either sham-treated ("control surgery") or treated with TBI. In the TBI group, TBI was immediately followed by a single injection into the impact site of DMSO, PAP2 alone, TAT alone, or PAP2-TAT. After this, animals were regularly monitored for weight loss and gait performance in the CatWalk XT Test over 7 days and histology at the terminal time-point (see Figure 6A).

First of all, we analyzed weight loss (Figure 6B). All animals, including sham-treated mice, lost weight in relation to their weight before TBI or sham surgery intervention (Figure 6B). Also, all animals gained weight between 6 h and 7 d after sham or TBI treatment without any specific impact by the PAP2-TAT peptide (Figure 6B). However, surprisingly, the TAT-treated group consistently had the least weight loss over the seven day observation period although with no statistical significance (Figure 6B). Thus, as noted for neuronal growth (Figure 3), the TAT peptide alone appears to exert some biological activity by itself.

Next, we employed CatWalk XT gait analysis to analyze the impact of PAP2-TAT on the recovery of gait parameters affected by TBI (Figure 6C−F). In all TBI-treated animals, the stand time of the right hindlimb was reduced compared to sham-treated animals at 1 day post injury, suggesting TBI-inflicted gait impairment irrespective of peptide or DMSO treatment (Figure 6C). The duty cycle (i.e., the ratio of stand time to step cycle; Figure 6D) was reduced by TBI at 1 day post injury for DMSO and PAP2 and TAT peptides alone. However, the PAP2-TAT-injected animals had values comparable to those of sham (Figure 6D). A similar trend without reaching significance was observed for the stride length (Figure 6E). After TBI, the stride length was increased in DMSO, PAP2, and TAT groups in relation to sham animals but not as much in PAP2-TAT-treated animals (Figure 6E). The print width of the paws was reduced by TBI in relation to sham in DMSO and PAP2 groups (Figure 6F). In contrast, not only PAP2-TAT but also TAT-treated animals showed a tendency toward maintaining the same paw width after TBI as before the intervention (Figure 6F).

Finally, the extent of TBI-associated neuroinflammation as revealed by astrocyte (labeled with GFAP) and microglia (labeled with IBA1) abundance in the cortex was assessed (Figure 6G−K). Both cell types were strongly induced by TBI in relation to sham-treated animals at 7 days post injury (Figure 6G−K). In animals experiencing TBI, no obvious difference for GFAP-(Figure 6J) or IBA1-positive (Figure 6K) cells was observed for all the peptide treatments in relation to DMSO (Figure 6J,K). This suggests no obvious impact of PAP2-TAT on TBI-associated neuroinflammatory responses under experimental conditions employed in this study. Finally, the wound area (see Figure 6H,I) in the cortex was quantified (Figure 6L). PAP2-TAT-treated animals had a reduced wound area compared to the other peptide treatments and DMSO, although this effect was not significant.

In summary, PAP2-TAT-mediated PTEN inhibition showed a trend toward elevating TBI's impact on selected gait parameters.

DISCUSSION

Effect of PAP2-TAT on Neuronal Growth, Growth Cones, and Synapse Formation

In this study, the potential of peptide-based PTEN inhibition as treatment for neuronal injury was further exploited. Using several neuronal cell types (SH-SY5Y, primary mouse neurons), we observed that two preconditions for peptide treatments were met with (i) low cell toxicity (up to 10 μM; Figure 1) and (ii) high percentage of penetration of PAP2-TAT into cells (Figures 1 and 2). Of note, high cell transfer was achieved even though peptide size was reduced through omission of four TAT flanking amino acids (see Table 1).

Enhanced neuronal growth of peripheral neurons was previously reported for PAP2.[25] In addition, PAP4 targeting PTEN's C-terminal domain stimulated central neuron growth.[25,26] Herein, we demonstrated that PAP2 targeting PTEN's phosphatase domain also stimulates central neuronal growth (Figure 3). Taken together, several PAPs targeting multiple PTEN domains interfere with PTEN function and stimulate the growth of primary central and peripheral neurons. Furthermore, our finding on an enhanced number of presynaptic marker decoration along dendrites (Figure 4) is in line with similar findings on PTEN deletion.[12,13]

Previously, genetic PTEN deletion resulted in larger growth cones.[5,6] In line with this, when PTEN was blocked by PAPs, as used in this study, growth cone size was also increased (Figure 3). Growth cone shape and motility are largely influenced by actin and microtubule dynamics.[35] For instance, increased growth cone size correlates with a decrease in neurite growth rate.[37] Notably, PTEN was previously associated with growth cone microtubule dynamics and posttranslational modification such as tyrosination.[7,38,39] Proper microtubule tyrosination and dynamics are required for neuronal growth.[40,41] Indeed, several approaches targeting microtubule function have proven successful to enhance axonal regeneration in mouse models.[38,42] Thus, PTEN deletion might alleviate a break on microtubule dynamics and modifications, allowing for more neuronal growth and regeneration.

Signaling Pathways Affected by PTEN Inhibition

The main signaling activity upregulated after the PTEN blockade is PI3 kinase signaling. In contrast, in the present work (Figure 5), P-AKT levels were only mildly affected. Since PTEN/PI3 kinase signaling acts upstream of many signaling pathways, including MAP kinases, other pathways may be

https://doi.org/10.1021/acs.biomac.6c00695
Biomacromolecules 2026, 27, 5419−5431

affected indirectly or in a cell-type-specific manner. Herein, we observed elevated P-ERK levels upon PAP2-mediated PTEN inhibition (Figure 5). This is in agreement with a previous study in the injured mouse spinal cord where PAP-mediated PTEN inhibition also elevated P-ERK abundance.[26] This suggests enhanced MAP kinase pathway signaling after PAP2-TAT-mediated PTEN inhibition.

So far, the connection between PTEN ablation and concomitant elevation of MAP kinase activity is less well studied, particularly in neurons. However, in cancer cells, PTEN downregulation is connected to enhanced ERK phosphorylation.[43−45] In neurons, PTEN overexpression caused P-ERK downregulation[46] which is congruent with our findings (Figure 5). MAP kinases are established targets in axonal regeneration.[47] Thus, in addition to P-AKT, our findings suggest that MAP kinases might emerge as a pathway involved in enhancing regeneration after PTEN inhibition.

Similar to the connection of PTEN deletion with MAP kinases, regulation of STAT transcription factors by PAP2-TAT (Figure 5) is not well-established so far. PAP2-TAT resulted in enhanced STAT phosphorylation suggesting more STAT activity after PTEN blockage (Figure 5). In few reports available in non-neuronal cells, PTEN was associated with JAK/STAT signaling.[48−50] In endothelial cells, JAK/STAT signaling was activated following PTEN silencing,[50] a finding in agreement with neurons analyzed in this study. Furthermore, autophosphorylation of CaMK2 (Phospho Thr 287; Figure 5D) known to activate CaMK2 activity was elevated by PAP2-TAT (Figure 5D). Notably, phospho-Thr287 levels of CaMK2 were previously reported to be enriched in growth cones and CaMK2 inhibition modulates growth cone collapse.[51] Thus, PAP2-mediated PTEN inhibition might exert its modulatory function on growth cones (Figure 3) through elevating Phospho-CaMK2 levels.

Taken together, our findings suggest an interaction of PTEN blockage with enhanced MAPK and STAT signaling.

PAP2-TAT Effects in a Mouse Model of TBI

So far, peptide-based PTEN blockage was not employed in mouse TBI models in contrast to compound-mediated and genetic inhibition, resulting in enhanced recovery for selected parameters.[17,19,21,22] As mentioned before, PAP2-TATs were successfully applied to enhance regeneration in mouse spinal cord injury models.[25,26,28] Here, two studies have shown behavior improvements of locomotor parameters (e.g., grid walk, stride length) by PAP-mediated PTEN inhibition.[25,28] In our study, we can confirm such a positive impact of PAPs on behavior parameters after neuronal injury (Figure 6). We observed positive effects of PAP2-TAT on the recovery of gait parameters which were impaired by TBI and reduction of the TBI-induced lesion site (Figure 6). Nevertheless, PAP2-TAT effects obtained were modest, and results frequently did not reach significance. One confounding factor contributing to this is the high variability in the TBI severity between animals. Furthermore, in previous studies mentioned above, PAP2-TATs were systemically and not locally injected, and injection was performed multiple times. This might result in a broader and more sustained PTEN inhibition in more (brain) cells over a longer time and therefore stronger effects in post-TBI recovery. However, given PTEN's function as a tumor suppressor gene, such systemic PTEN inhibition particularly in proliferating cells might pose the risk of tumor formation as shown in a previous report in adult mice with long-term genetic PTEN ablation.[4] One possibility to circumvent systemic PTEN inhibition would have been delivery via mini-pump infusion over 1−3 weeks directly into the brain. While future experiments have to underscore the potential of PAP2-TATs to enhance regeneration after brain injury in rodent models, this study provides first hints that PAP2-TAT might be a promising tool for such translational approaches.

LIMITATIONS

In this study, we noted that the TAT sequence alone resulted in some biological activity, e.g., on neuronal growth and growth cone morphology (Figure 3). These effects by TAT alone were, in general, weaker, or, in some assays, even absent (e.g., Figure 4) compared to PAP2-TAT showing that the biological activity achieved was mainly exerted through PAP2-mediated PTEN inhibition. However, our data clearly point toward the necessity of including a control group of TAT alone when performing experiments with TAT fusion peptides.

For the phosphor-array, we only provided $N = 1$ since many animals had to be pooled to obtain sufficient material (see Materials and Methods). Thus, we did not provide sufficient N-numbers for statistical testing. However, using immunocytochemistry, we were able to independently confirm P-STAT regulation by PAP2-TAT as one of the candidate molecules (Figure 4).

CONCLUSIONS

In this study, we have shown that peptide-based PTEN inhibition through PAP2-TAT enhances neuronal growth and growth cone size. This points to a potential PAP2-TAT function in stimulating regrowth of severed axons after CNS injury. So far, PAP2-TAT has not been investigated in TBI. In a rodent weight-drop TBI model, a single PAP2-TAT injection into the lesion site immediately after TBI slightly modulated some TBI-impaired gait parameters. This suggests that single or multiple PAP2-TAT injections after TBI might be an interesting approach to enhance neuronal growth, thereby reducing TBI-associated impairments in, e.g., motor function.

ASSOCIATED CONTENT

Data Availability Statement

The data that support the findings of this study are available from the corresponding author upon reasonable request.

Supporting Information

The Supporting Information is available free of charge at https://pubs.acs.org/doi/10.1021/acs.biomac.6c00695.

Supporting Figure 1: a reaction scheme for the fluorescein-labeled peptides; Supporting Figure S2: mass spectra of the peptides by MALDI-ToF MS; and Supporting Figure S3: liquid chromatograms for the peptides (PDF)

AUTHOR INFORMATION

Corresponding Authors

Christopher V. Synatschke − *Max Planck Institute for Polymer Research, Mainz 55128, Germany*; Email: synatschke@mpip-mainz.mpg.de

Bernd Knöll − *Institute of Neurobiochemistry, Ulm University, Ulm 89081, Germany*; orcid.org/0000-0001-7685-3796; Email: bernd.knoell@uni-ulm.de

https://doi.org/10.1021/acs.biomac.6c00695
Biomacromolecules 2026, 27, 5419−5431

Authors

Karla K. Rivera − *Institute of Neurobiochemistry, Ulm University, Ulm 89081, Germany*

Yu-Liang Tsai − *Max Planck Institute for Polymer Research, Mainz 55128, Germany*

Jialei Song − *Institute of Neurobiochemistry, Ulm University, Ulm 89081, Germany*

Hao Gu − *Institute of Neurobiochemistry, Ulm University, Ulm 89081, Germany*

Anne-Sophie Gutt − *Institute of Neurobiochemistry, Ulm University, Ulm 89081, Germany*

Daniela Sinske − *Institute of Neurobiochemistry, Ulm University, Ulm 89081, Germany*

Claudia Klugmann − *Institute of Neurobiochemistry, Ulm University, Ulm 89081, Germany*

Marica Pagliarini − *German Center for Neurodegenerative Diseases-DZNE, Ulm 89081, Germany; Department of Neurology, Ulm University, Ulm 89081, Germany*

Francesco Roselli − *German Center for Neurodegenerative Diseases-DZNE, Ulm 89081, Germany; Department of Neurology, Ulm University, Ulm 89081, Germany;* orcid.org/0000-0001-9935-6899

Complete contact information is available at: https://pubs.acs.org/10.1021/acs.biomac.6c00695

Author Contributions

[⊥]BK, CVS, and FR conceived the study and supervised the project. KR, YLT, CK, DS, HG, and MP performed experiments and data analysis. BK prepared figures and drafted the manuscript. All authors read and approved the manuscript.

Funding

This work was supported by the Deutsche Forschungsgemeinschaft (DFG, German Research Foundation) through the grant No. 441734479 to BK and CVS. BK and FR are in addition funded by the DFG-Project-ID 251293561-SFB 1149. FR is also funded by the BMBF (through the JPND initiative, "DC4MND" consortium, grant no. BMBF-01ED2301).

Notes

Ethics approval and consent to participate. All experimental procedures were approved by the regional authority (Regierungspräsidium Tübingen, Germany).
The authors declare no competing financial interest.

■ ACKNOWLEDGMENTS

We thank the scientific support from the Biocore and Mass Spectrometry facilities at the Max Planck Institute for Polymer Research. In addition, we thank the IMB Microscopy Core Facility for the use of their instruments. Funding of the German Research Foundation supported the Stellaris 8 FALCON (P# 497669232, Leica, IMB, Mainz).

■ REFERENCES

(1) Fuchs, J.; Eickholt, B. J.; Leondaritis, G. Harnessing PTEN's Growth Potential in Neuronal Development and Disease. *Neurosci Insights* **2020**, *15*, 2633105520959056.

(2) Skelton, P. D.; Stan, R. V.; Luikart, B. W. The Role of PTEN in Neurodevelopment. *Complex Psychiatry* **2020**, *5*, 60−71.

(3) Chen, Y.; Huang, W. C.; Sejourne, J.; Clipperton-Allen, A. E.; Page, D. T. Pten Mutations Alter Brain Growth Trajectory and Allocation of Cell Types through Elevated beta-Catenin Signaling. *J. Neurosci.* **2015**, *35* (28), 10252−10267.

(4) Meyer Zu Reckendorf, S.; Moser, D.; Blechschmidt, A.; Joga, V. N.; Sinske, D.; Hegler, J.; Deininger, S.; Catanese, A.; Vettorazzi, S.; Antoniadis, G.; Boeckers, T.; Knoll, B. Motoneuron-Specific PTEN Deletion in Mice Induces Neuronal Hypertrophy and Also Regeneration after Facial Nerve Injury. *J. Neurosci.* **2022**, *42* (12), 2474−2491.

(5) Ning, K.; Drepper, C.; Valori, C. F.; Ahsan, M.; Wyles, M.; Higginbottom, A.; Herrmann, T.; Shaw, P.; Azzouz, M.; Sendtner, M. PTEN depletion rescues axonal growth defect and improves survival in SMN-deficient motor neurons. *Hum. Mol. Genet.* **2010**, *19* (16), 3159−3168.

(6) Oinuma, I.; Ito, Y.; Katoh, H.; Negishi, M. Semaphorin 4D/Plexin-B1 stimulates PTEN activity through R-Ras GTPase-activating protein activity, inducing growth cone collapse in hippocampal neurons. *J. Biol. Chem.* **2010**, *285* (36), 28200−28209.

(7) Getz, S. A.; Tariq, K.; Marchand, D. H.; Dickson, C. R.; Howe Vi, J. R.; Skelton, P. D.; Wang, W.; Li, M.; Barry, J. M.; Hong, J.; Luikart, B. W. PTEN Regulates Dendritic Arborization by Decreasing Microtubule Polymerization Rate. *J. Neurosci.* **2022**, *42* (10), 1945−1957.

(8) Kwon, C. H.; Luikart, B. W.; Powell, C. M.; Zhou, J.; Matheny, S. A.; Zhang, W.; Li, Y.; Baker, S. J.; Parada, L. F. Pten regulates neuronal arborization and social interaction in mice. *Neuron* **2006**, *50* (3), 377−388.

(9) Christie, K. J.; Webber, C. A.; Martinez, J. A.; Singh, B.; Zochodne, D. W. PTEN inhibition to facilitate intrinsic regenerative outgrowth of adult peripheral axons. *J. Neurosci.* **2010**, *30* (27), 9306−9315.

(10) Kath, C.; Goni-Oliver, P.; Muller, R.; Schultz, C.; Haucke, V.; Eickholt, B.; Schmoranzer, J. PTEN suppresses axon outgrowth by down-regulating the level of detyrosinated microtubules. *PLoS One* **2018**, *13* (4), No. e0193257.

(11) Tariq, K.; Cullen, E.; Getz, S. A.; Conching, A. K. S.; Goyette, A. R.; Prina, M. L.; Wang, W.; Li, M.; Weston, M. C.; Luikart, B. W. Disruption of mTORC1 rescues neuronal overgrowth and synapse function dysregulated by Pten loss. *Cell Rep.* **2022**, *41* (5), 111574.

(12) Luikart, B. W.; Zhang, W.; Wayman, G. A.; Kwon, C. H.; Westbrook, G. L.; Parada, L. F. Neurotrophin-dependent dendritic filopodial motility: a convergence on PI3K signaling. *J. Neurosci.* **2008**, *28* (27), 7006−7012.

(13) Williams, M. R.; DeSpenza, T., Jr.; Li, M.; Gulledge, A. T.; Luikart, B. W. Hyperactivity of newborn Pten knock-out neurons results from increased excitatory synaptic drive. *J. Neurosci.* **2015**, *35* (3), 943−959.

(14) Yonan, J. M.; Chen, K. D.; Baram, T. Z.; Steward, O. PTEN deletion in the adult dentate gyrus induces epilepsy. *Neurobiol. Dis.* **2024**, *203*, 106736.

(15) Gutilla, E. A.; Steward, O. Selective neuronal PTEN deletion: can we take the brakes off of growth without losing control? *Neural Regen Res.* **2016**, *11* (8), 1201−1203.

(16) Borges, G. A.; Webber, L. P.; M Marques, A. E.; Guerra, E. N.; Castilho, R. M.; Squarize, C. H. Pharmacological PTEN inhibition: potential clinical applications and effects in tissue regeneration. *Regen Med.* **2020**, *15* (2), 1329−1344.

(17) Liu, K.; Lu, Y.; Lee, J. K.; Samara, R.; Willenberg, R.; Sears-Kraxberger, I.; Tedeschi, A.; Park, K. K.; Jin, D.; Cai, B.; Xu, B.; Connolly, L.; Steward, O.; Zheng, B.; He, Z. PTEN deletion enhances the regenerative ability of adult corticospinal neurons. *Nat. Neurosci.* **2010**, *13* (9), 1075−1081.

(18) Ohtake, Y.; Hayat, U.; Li, S. PTEN inhibition and axon regeneration and neural repair. *Neural Regen Res.* **2015**, *10* (9), 1363−1368.

(19) Ding, J.; Guo, J.; Yuan, Q.; Yuan, F.; Chen, H.; Tian, H. Inhibition of phosphatase and tensin homolog deleted on chromosome 10 decreases rat cortical neuron injury and blood-brain barrier permeability, and improves neurological functional recovery in traumatic brain injury model. *PLoS One* **2013**, *8* (11), No. e80429.

(20) Liu, R.; Liao, X. Y.; Tang, J. C.; Pan, M. X.; Chen, S. F.; Lu, P. X.; Lu, L. J.; Zhang, Z. F.; Zou, Y. Y.; Bu, L. H.; Qin, X. P.; Wan, Q. BpV(pic) confers neuroprotection by inhibiting M1 microglial polarization and MCP-1 expression in rat traumatic brain injury. *Mol. Immunol.* **2019**, *112*, 30−39.
(21) Pearson, A.; Ortiz, C.; Eisenbaum, M.; Arrate, C.; Browning, M.; Mullan, M.; Bachmeier, C.; Crawford, F.; Ojo, J. O. Deletion of PTEN in microglia ameliorates chronic neuroinflammation following repetitive mTBI. *Mol. Cell. Neurosci.* **2023**, *125*, 103855.
(22) Shi, Z.; Mao, L.; Chen, S.; Du, Z.; Xiang, J.; Shi, M.; Wang, Y.; Wang, Y.; Chen, X.; Xu, Z. X.; Gao, Y. Reversing Persistent PTEN Activation after Traumatic Brain Injury Fuels Long-Term Axonal Regeneration via Akt/mTORC1 Signaling Cascade. *Adv. Sci.* **2025**, *12* (6), No. e2410136.
(23) Tsai, Y.-L.; Song, J.; Shi, R.; Knoll, B.; Synatschke, C. V. A Roadmap of Peptide-Based Materials in Neural Regeneration. *Adv. Healthc Mater.* **2025**, *14* (2), No. e2402939.
(24) Spinelli, L.; Lindsay, Y. E.; Leslie, N. R. PTEN inhibitors: an evaluation of current compounds. *Adv. Biol. Regul.* **2015**, *57*, 102−111.
(25) Ohtake, Y.; Park, D.; Abdul Muneer, P. M.; Li, H.; Xu, B.; Sharma, K.; Smith, G. M.; Selzer, M. E.; Li, S. The effect of systemic PTEN antagonist peptides on axon growth and functional recovery after spinal cord injury. *Biomaterials* **2014**, *35* (16), 4610−4626.
(26) Bhowmick, S.; Muneer, P. M. A. PTEN Blocking Stimulates Corticospinal and Raphespinal Axonal Regeneration and Promotes Functional Recovery After Spinal Cord Injury. *J. Neuropathol. Exp. Neurol.* **2021**, *80* (2), 169−181.
(27) Cheng, L.; Sami, A.; Ghosh, B.; Goudsward, H. J.; Smith, G. M.; Wright, M. C.; Li, S.; Lepore, A. C. Respiratory axon regeneration in the chronically injured spinal cord. *Neurobiol. Dis.* **2021**, *155*, 105389.
(28) Michel-Flutot, P.; Cheng, L.; Thomas, S. J.; Lisi, B.; Schwartz, H.; Lam, S.; Lyttle, M.; Jaffe, D. A.; Smith, G.; Li, S.; Wright, M. C.; Lepore, A. C. PTEN inhibition promotes robust growth of bulbospinal respiratory axons and partial recovery of diaphragm function in a chronic model of cervical contusion spinal cord injury. *Exp. Neurol.* **2024**, *378*, 114816.
(29) Urban, M. W.; Ghosh, B.; Block, C. G.; Strojny, L. R.; Charsar, B. A.; Goulao, M.; Komaravolu, S. S.; Smith, G. M.; Wright, M. C.; Li, S.; Lepore, A. C. Long-Distance Axon Regeneration Promotes Recovery of Diaphragmatic Respiratory Function after Spinal Cord Injury. *eNeuro* **2019**, *6* (5), No. ENEURO.0096−19.2019.
(30) Reiners, J. C.; Leopold, L.; Hallebach, V.; Sinske, D.; Meier, P.; Amoroso, M.; Langgartner, D.; Reber, S. O.; Knoll, B. Acute stress modulates the outcome of traumatic brain injury-associated gene expression and behavioral responses. *FASEB J.* **2023**, *37* (11), No. e23218.
(31) Gu, H.; Reiners, J. C.; Sinske, D.; Reber, S. O.; Knoll, B. Previous exposure to traumatic brain injury alters acute stress responses in mice. *Sci. Rep* **2025**, *15* (1), 42565.
(32) Jullian, M.; Hernandez, A.; Maurras, A.; Puget, K.; Amblard, M.; Martinez, J.; Subra, G. N-terminus FITC labeling of peptides on solid support: the truth behind the spacer. *Tetrahedron Lett.* **2009**, *50* (3), 260−263.
(33) Hemström, P.; Irgum, K. Hydrophilic interaction chromatography. *J. Sep. Sci.* **2006**, *29* (12), 1784−1821.
(34) Meloni, B. P.; Craig, A. J.; Milech, N.; Hopkins, R. M.; Watt, P. M.; Knuckey, N. W. The neuroprotective efficacy of cell-penetrating peptides TAT, penetratin, Arg-9, and Pep-1 in glutamic acid, kainic acid, and in vitro ischemia injury models using primary cortical neuronal cultures. *Cell. Mol. Neurobiol.* **2014**, *34* (2), 173−181.
(35) Bradke, F.; Fawcett, J. W.; Spira, M. E. Assembly of a new growth cone after axotomy: the precursor to axon regeneration. *Nat. Rev. Neurosci.* **2012**, *13* (3), 183−193.
(36) Chwin, N.; Kiryk, A. The integral role of PTEN in brain function: from neurogenesis to synaptic plasticity and social behavior. *Acta Neurobiol Exp (Wars)* **2025**, *84* (4), 309−318.
(37) Ren, Y.; Suter, D. M. Increase in Growth Cone Size Correlates with Decrease in Neurite Growth Rate. *Neural Plast.* **2016**, *2016*, 3497901.
(38) Leibinger, M.; Zeitler, C.; Paulat, M.; Gobrecht, P.; Hilla, A.; Andreadaki, A.; Guthoff, R.; Fischer, D. Inhibition of microtubule detyrosination by parthenolide facilitates functional CNS axon regeneration. *eLife* **2023**, *12*, RP88279.
(39) Kreis, P.; Leondaritis, G.; Lieberam, I.; Eickholt, B. J. Subcellular targeting and dynamic regulation of PTEN: implications for neuronal cells and neurological disorders. *Front. Mol. Neurosci.* **2014**, *7*, 23.
(40) Marcos, S.; Moreau, J.; Backer, S.; Job, D.; Andrieux, A.; Bloch-Gallego, E. Tubulin tyrosination is required for the proper organization and pathfinding of the growth cone. *PLoS One* **2009**, *4* (4), No. e5405.
(41) Challacombe, J. F.; Snow, D. M.; Letourneau, P. C. Dynamic microtubule ends are required for growth cone turning to avoid an inhibitory guidance cue. *J. Neurosci.* **1997**, *17* (9), 3085−3095.
(42) Hellal, F.; Hurtado, A.; Ruschel, J.; Flynn, K. C.; Laskowski, C. J.; Umlauf, M.; Kapitein, L. C.; Strikis, D.; Lemmon, V.; Bixby, J.; Hoogenraad, C. C.; Bradke, F. Microtubule stabilization reduces scarring and causes axon regeneration after spinal cord injury. *Science* **2011**, *331* (6019), 928−931.
(43) Ebbesen, S. H.; Scaltriti, M.; Bialucha, C. U.; Morse, N.; Kastenhuber, E. R.; Wen, H. Y.; Dow, L. E.; Baselga, J.; Lowe, S. W. Pten loss promotes MAPK pathway dependency in HER2/neu breast carcinomas. *Proc. Natl. Acad. Sci. U. S. A.* **2016**, *113* (11), 3030−3035.
(44) Deb, T. B.; Barndt, R. J.; Zuo, A. H.; Sengupta, S.; Coticchia, C. M.; Johnson, M. D. PTEN-mediated ERK1/2 inhibition and paradoxical cellular proliferation following Pnck overexpression. *Cell Cycle* **2014**, *13* (6), 961−973.
(45) Chetram, M. A.; Hinton, C. V. PTEN regulation of ERK1/2 signaling in cancer. *J. Recept Signal Transduct Res.* **2012**, *32* (4), 190−195.
(46) Lee, J. E.; Lim, M. S.; Park, J. H.; Park, C. H.; Koh, H. C. PTEN Promotes Dopaminergic Neuronal Differentiation Through Regulation of ERK-Dependent Inhibition of S6K Signaling in Human Neural Stem Cells. *Stem Cells Transl. Med.* **2016**, *5* (10), 1319−1329.
(47) Lin, F. X.; Gu, H. Y.; He, W. MAPK signaling pathway in spinal cord injury: Mechanisms and therapeutic potential. *Exp. Neurol.* **2025**, *383*, 115043.
(48) Zhou, J.; Wulfkuhle, J.; Zhang, H.; Gu, P.; Yang, Y.; Deng, J.; Margolick, J. B.; Liotta, L. A.; Petricoin, E.; Zhang, Y. Activation of the PTEN/mTOR/STAT3 pathway in breast cancer stem-like cells is required for viability and maintenance. *Proc. Natl. Acad. Sci. U. S. A.* **2007**, *104* (41), 16158−16163.
(49) Wu, R.; Sun, S.; Steinberg, B. M. Requirement of STAT3 activation for differentiation of mucosal stratified squamous epithelium. *Mol. Med.* **2003**, *9* (3−4), 77−84.
(50) Jiao, J.; Zhang, D.; Peng, J.; Li, Y. MDM2 interacts with PTEN to inhibit endothelial cell development and promote deep vein thrombosis via the JAK/STAT signaling pathway. *Mol. Med. Rep.* **2024**, *31* (2), 31.
(51) Easley, C. A.; Faison, M. O.; Kirsch, T. L.; Lee, J. A.; Seward, M. E.; Tombes, R. M. Laminin activates CaMK-II to stabilize nascent embryonic axons. *Brain Res.* **2006**, *1092* (1), 59−68.

https://doi.org/10.1021/acs.biomac.6c00695
Biomacromolecules 2026, 27, 5419−5431